49th SME North American Manufacturing Research Conference, NAMRC 49, Ohio, USA

Propagation of Johnson-Cook flow stress model uncertainty to milling force uncertainty using finite element analysis and time domain simulation

[a]Timothy No, [a,b]Michael Gomez, [b]Jaydeep Karandikar, [c]Jarred Heigel, [a]Ryan Copenhaver, [a,b]Tony Schmitz[*]

[a]University of Tennessee, Knoxville, TN, 37996, USA
[b]Manufacturing Science Division, Oak Ridge National Laboratory, Oak Ridge, TN, 37831 USA
[c]Third Wave Systems, Eden Prairie, MN, 55344, USA

* Corresponding author. Tel.: +1-865-974-6141; fax: +1-865-974-5274. E-mail address: tony.schmitz@utk.edu

Abstract

This paper describes the propagation of uncertainty in the parameters for a 6061-T6 aluminum Johnson-Cook flow stress model to, first, the uncertainty in the corresponding mechanistic cutting force model obtained by orthogonal cutting finite element simulation and, second, the milling force predicted by time domain simulation using the force model. The approach includes five key elements: 1) a literature review to identify the means and standard deviations for the 6061-T6 aluminum Johnson-Cook model parameters; 2) structured light scanning to measure an endmill's cutting edge macro-geometry along the tool axis; 3) structured light scanning to identify the cutting edge cross-sectional rake and relief profiles for the same endmill; 4) orthogonal cutting finite element analysis to determine the mechanistic force model coefficients that relate the force components to chip area and width using the tool's rake and relief profiles and random samples from the Johnson-Cook parameter distributions; and 5) time domain simulation with inputs that include the measured cutting edge macro-geometry, uncertain finite element-based force model, and measured structural dynamics. Distributions for milling force predictions are determined by Monte Carlo simulation and compared to in-process measurements for an indexable endmill-collet holder to demonstrate the approach. It is observed that 95% confidence intervals on the predicted forces bound the measured time-dependent force profile peaks in over half of the cases tested. It is also seen that the Johnson-Cook flow stress model-based force predictions performed as well as predictions based on a calibrated mechanistic force model.

1. Introduction

Digital modeling is increasingly the industry standard for part production by milling. Three-dimensional computer-aided design (CAD)/computer-aided manufacturing (CAM) is the norm, where component solid models are used to generate computer numerically controlled (CNC) part programs by the part programmer. The corresponding M/G code instructions define the machine motions required to remove material from the block, forging, casting, or additively manufactured preform using the selected rotating endmill. The end goal is a component with the desired geometry and surface finish obtained from the first trial onward.

Digital modeling is also applied to aid in selection of operating parameters that result in a process that repeatably produces in-tolerance parts at maximum profit. For milling, this

modeling includes the process dynamics, which encompasses both stability (i.e., stable operation, which exhibits only forced vibration, versus unstable performance that demonstrates self-excited vibration or period-n bifurcations and the corresponding degradation in part quality) and surface location error, or part geometry errors that occur due to the phasing between the tool-part relative motions and the instant the final surface is generated [1-3]. In both cases, the required modeling inputs are: 1) the tool geometry; 2) the force model that relates the cutting force required to shear away the material to the commanded chip dimensions; and 3) the structural dynamics of the tool-holder-spindle-machine-workpiece combination. The importance of this digital approach is underscored in a World Economic Forum report on the COVID-19 crisis and its effect on manufacturing. It states that: "Industry 4.0 technologies are necessary for survival in a global marketplace that will require more agile and flexible production systems and supply chains" and "manufacturers will see the benefits of applying a digital-first mindset to a physical business" [4].

In this paper, a digital modeling framework for milling force that includes: structured light scanning to identify the endmill's cutting edge macro-geometry along the tool axis; structured light scanning to measure the rake and relief profiles; commercially-available finite element analysis of orthogonal cutting to determine the mechanistic force model coefficients using the work material's constitutive model and tool's rake and relief edge geometries; and time domain simulation with inputs that include the cutting edge macro-geometry, force model, and tool tip frequency response function (FRF). The outcome is the ability to predict milling force (and vibration) for any endmill-work material combination in an integrated digital approach. An indexable endmill is selected for experimental validation, but the approach is generic to any endmill geometry and peripheral milling process. A primary contribution of this paper is the propagation of uncertainties in the 6061-T6 aluminum Johnson-Cook flow stress model parameters to uncertainty in the predicted time-dependent milling force using both finite element analysis and time domain simulation.

2. Background

Modeling of machining operations has received continuous international attention since the mid-20th century [1-3]. A subset of these efforts has included a specific focus on modeling the performance based on the endmill geometry. For example, multiple authors have modeled the performance of indexable cutters, which are considered in this study. Fu *et al.* predicted the forces in face milling for various cutting conditions and cutter geometries [5]. Kim and Ehmann simulated the static and dynamic cutting forces in face milling [6]. Zheng *et al.* modeled face milling as the simultaneous action of multiple single point cutting tools [7]. Engin and Altintas presented a generalized indexable cutter model for predicting cutting force, vibration, surface finish, and stability in milling, where the cutting edge locations were defined mathematically [8-9].

Authors have also examined non-standard cutting edge geometries. Wang and Yang [10] presented force models in the angle and frequency domains for a cylindrical roughing endmill

with sinusoidal cutting edges. Merdol and Altintas [11] modeled the serration profile by fitting points along a cubic spline projected on the helical flutes. This geometric model was used to generate a time domain milling model. Dombovari *et al.* [12] used the semi-discretization method to analyze the stability of serrated endmills. Later, he and others created general models for various tool geometries [13-14]. Koca and Budak [15] used a linear edge-force model and the semi-discretization method for force and stability modeling and optimized the serration waveform shape to reduce milling forces and increase stability. Grabowski *et al.* [16] extended their mechanistic model to calculate the process forces of serrated endmills. Tehranizadeh and Budak [17] proposed a genetic algorithm to optimize the design of serration shapes. No *et al.* performed force and stability modeling for non-standard geometry endmills [18-19].

Nomenclature

r	radius of point on end mill cutting edge
ϕ	angle of point on end mill cutting edge
z	position along end mill axis
$\Delta\phi$	angular resolution in time domain simulation
SR	steps per revolution in time domain simulation
RO	runout for point on end mill cutting edge
F_t	tangential component of cutting force
F_n	normal component of cutting force
k_{tc}	cutting force coefficient for tangential component
k_{nc}	cutting force coefficient for normal component
k_{te}	edge effect force coefficient for tangential component
k_{ne}	edge effect force coefficient for normal component
m	modal mass
c	modal viscous damping coefficient
k	modal stiffness
x	feed direction for end milling operation
y	perpendicular direction to x in the cut plane
F_x	x component of cutting force
F_y	y component of cutting force

This paper builds on prior efforts by implementing scanning metrology to measure the cutting edge macro-geometry and cross-sectional profile, applying finite element analysis to determine the force model by direct use of the measured edge rake and relief angle geometry, measuring the tool point dynamics, and including all three within a time domain simulation to enable digital force prediction. The specific aim is to begin with a Johnson-Cook flow stress model described by five parameters and their uncertainties, then propagate those uncertainties to an uncertain mechanistic cutting force model using finite element analysis of orthogonal cutting and the endmill's cutting edge geometry, and finally use Monte Carlo sampling to determine the variation in predicted time-dependent milling force based on the probabilistic force model and, by extension, the uncertain Johnson-Cook flow stress model.

3. Scanning metrology for edge geometry

To model the performance of endmills without requiring a model of the tool geometry from the manufacturer, scanning metrology is leveraged in this study. Structured light, or fringe, projection is applied to collect point clouds from the complex indexable endmill surfaces. While many commercial options are available, the GOM ATOS Compact Scan system was used for this research. The measurements proceeded by first preparing the indexable endmill surface using a removable anti-glare coating and attaching reference targets to the shank surface to enable multiple measurements to be stitched together and generate the solid model. Second, multiple scans were completed to obtain the point cloud and 3D model [18-19].
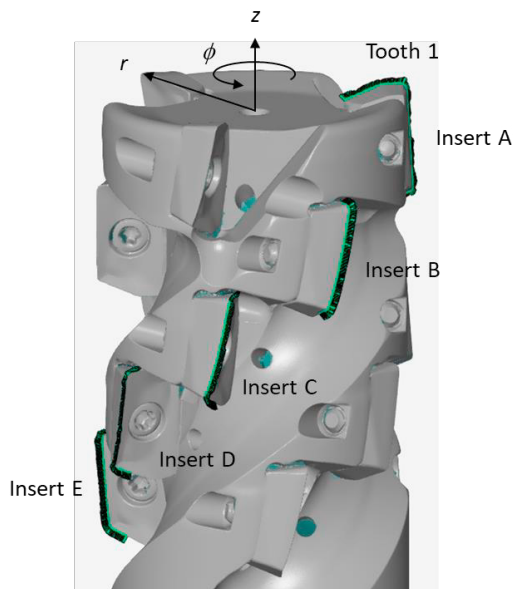

Figure 1: Scan and edge coordinates for one tooth on the indexable, square shoulder, helical endmill (31.75 mm shank and cut diameters, three teeth, 15 inserts total).

The procedure used to extract the edge coordinates from the solid model included four steps. First, using the best fit cylinder to the tool shank and the inserted end's extreme point, the origin was established on the tool's center line. Second, the points located on the insert cutting edges were selected. This step required manual manipulation within the GOM software. Third, the radius, r, and angle, ϕ, for each edge point was calculated in the local coordinate system. The teeth angles were normalized to a selected tooth and constrained to values between 0 and 360 deg; the z value was retained to obtain a triplet, $\{r, \phi, z\}$ for each point. Fourth, because the point density was higher than required for the time domain simulation, linear interpolation was used to obtain the triplet for axial slices located every 0.1 mm over the full cutting length; see Fig. 1, which displays the edge points for the Kennametal indexable, square shoulder, helical endmill (part number 3746099, three teeth, 31.75 mm shank and cut diameters, 111 mm overall length, and 44.8 mm maximum cut depth). The 15 inserts (three

"teeth" with five inserts each) were Kennametal EP1008 HD Grade KC725M carbide milling inserts with a TiN/TiCN/TiN coating (part number 3641734, 3.8 mm thickness, and 0.8 mm corner radius).
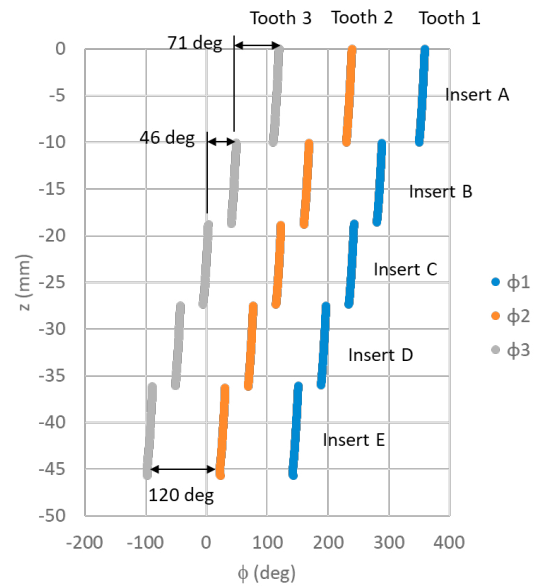

Figure 2: Insert angles, ϕ, for the three teeth calculated from the edge coordinates identified in Fig. 1.
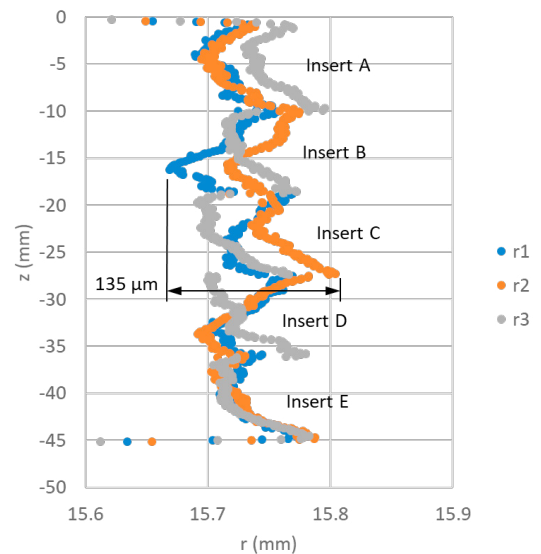

Fig. 3. Insert radii obtained from the edge coordinates identified in Fig. 1.

Example insert angle results are provided in Fig. 2. It is observed that the inserts are equally spaced at nominally 120 deg around the endmill periphery and that the angular offset between rows A and B (71 deg) differs from the offsets

between rows B and C, C and D, and D and E (46 deg). Radius results are displayed in Fig. 3. It is seen that each insert has a characteristic "U" shape with a smaller radius at the center and higher radii at the ends. The total variation in radii (excluding the rounded edges) across all 15 inserts is 135 μm. The runout contributes to the final force profile and must be incorporated for accurate force predictions.
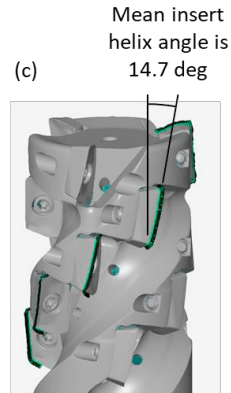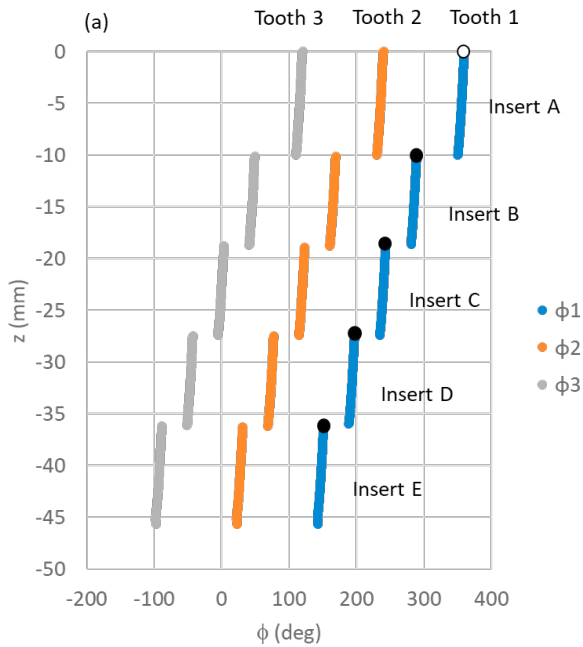

Figure 4: (a) Tip points on each insert were selected to calculate the global helix angles. The points are shown for tooth 1. (b) Global helix angles; two are identified due to the different angular offsets between rows A and B and the other pairs. (c) Mean helix angle for each insert.

The helix angles are described in Fig. 4. There are three primary angles. First, each insert is inclined with a mean helix angle of 14.7 deg. Second, two "global" helix angles can be identified. The first is due to the 71 deg angular offset between rows A and B. By unwrapping the cutter's periphery into a planar representation, the associated helix angle was obtained from the slope of a line that connected the tips of the two inserts. This helix angle is 62.6 deg. The second helix angle is provided by the 46 deg angular offset between the other pairs of insert rows and the corresponding best fit line's slope. This angle is 55.5 deg.

4. Scanning metrology for rake and relief profiles

Similar to the previous analysis, a coordinate system was established by fitting a cylinder to the tool shank and defining a plane at the fluted end's extreme point. The intersection of the cylinder's axis and the plane was set as the origin of the coordinate system. Planar cross-sections were then created along the tool's axis (z direction). Each section contained the rake and relief profiles of the three inserts at the corresponding axial location; an example section is displayed in Fig. 5.
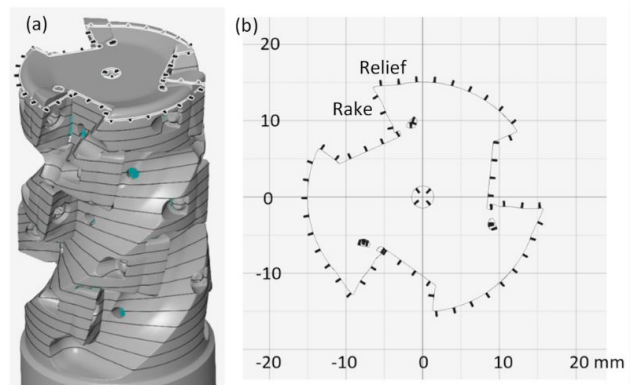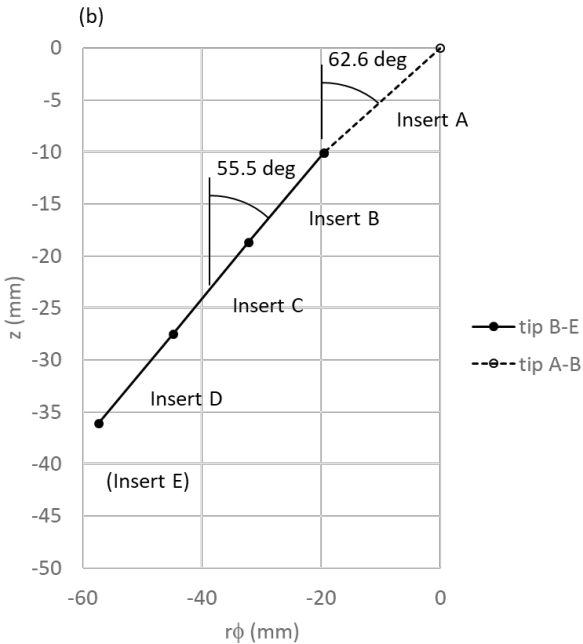

Figure 5: (a) Planar cross-sections of 3D model. (b) $z = -2$ mm section showing rake and relief faces of insert A for all three teeth.
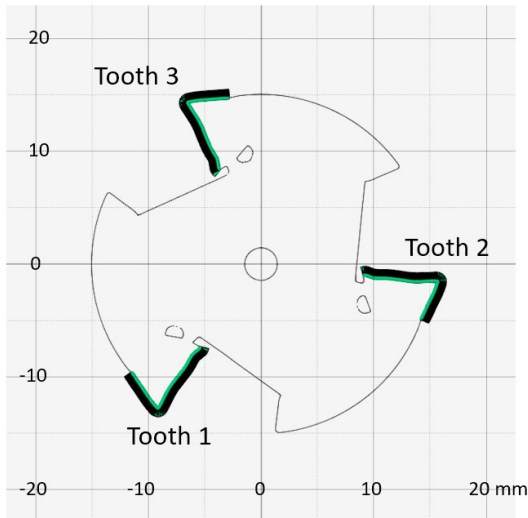
Figure 6: Rake and relief points on insert A of each tooth for the z = -2 mm section.
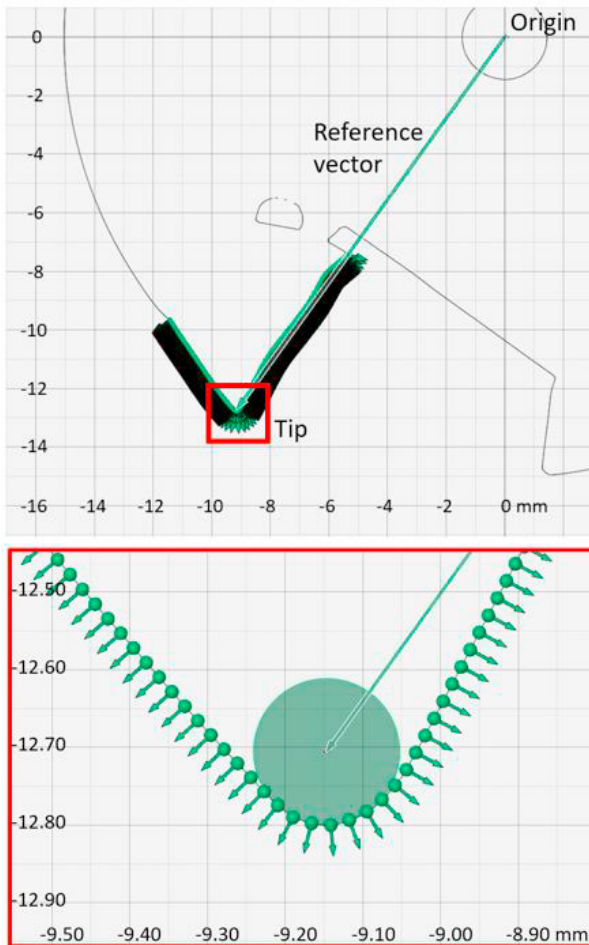

Figure 7: Reference vector for rake and relief angles. (Inset) tip details of tooth 1, insert A for the z = -2 mm section.

To calculate the spatially-dependent rake and relief angles, equidistant points were placed along the rake and relief profiles; see Fig. 6, where the spacing between each point is 0.025 mm. Each point had an $\{x, y, z\}$ coordinate and unit normal vector. A reference vector was created by connecting the origin of the section to the center of the best-fit circle at the tooth tip, where the rake and relief profiles meet (Fig. 7). To measure the rake angles, the unit normal vectors along the rake profile were rotated 90 deg clockwise to become unit tangent vectors. The rake angle was the angle between the tangent vector and reference vector. The same method was used to calculate the relief angles except the reference vector was now perpendicular (rotated 90 deg) to the original.

The rake and relief angles were plotted with respect to point distance, which is the distance traversed along the rake or relief profile from tip to point. A point at the tip was selected as the zero point so the distance of each subsequent point, moving away from the tip, could be calculated based on the equidistant point spacing. The rake and relief plots for tooth 1, insert A are shown in Figs. 8 and 9. The rake angle varies between negative and positive as it wraps around the radius of the tip and moves along the concave rake profile. The relief angle plot shows that the relief profile is initially curvilinear and then becomes linear.
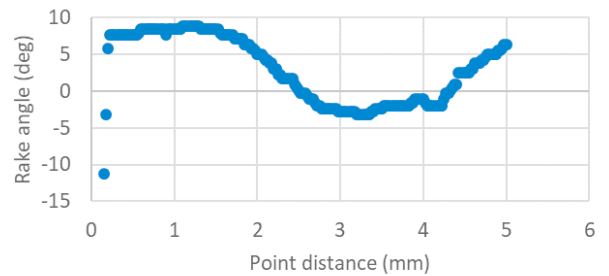
Figure 8: Tooth 1, insert A rake angle measurements for the z = -2 mm section.
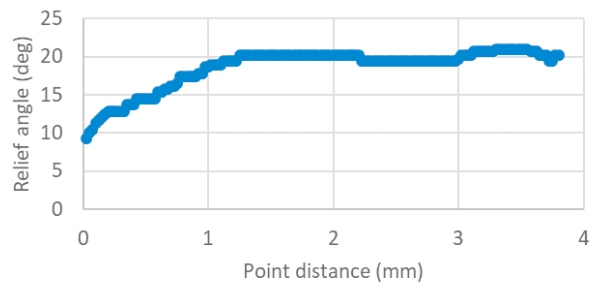
Figure 9: Tooth 1, insert A relief angle measurements for the z = -2 mm section.

5. Time domain simulation

Time domain simulation enables numerical solution of the coupled, second-order, time-delay differential equations of motion for milling in small time steps [1-2]. It is well suited to incorporating the inherent complexities of milling dynamics, including complicated tool geometries (runout of the cutter teeth, non-uniform teeth spacing, variable helix, and indexable

geometries) and the nonlinearity that occurs if the tooth leaves the cut due to large magnitude vibrations. The simulation applied here is based on the regenerative force, dynamic deflection model described by Smith and Tlusty [20]. As opposed to analytical or semi-analytical stability maps that provide a global picture of the stability behavior, time domain simulation provides information regarding the local cutting force and vibration behavior for the selected cutting conditions. The simulation used in this study is described in the following paragraphs; it was previously validated for serrated cutter geometries [18-19].

The time domain simulation directly incorporated the measured tooth angles and radius variation displayed in Figs. 2 and 3. For the tooth angles, the measured angles from the scanned edge were arranged in an array, where the columns were the individual teeth and the rows were the z locations (in steps of 0.1 mm). A row array of closely spaced tooth angles for use in the time domain simulation was then defined. The resolution in this array was: $\Delta\phi = 360/SR$, where SR is the number of steps per revolution in the simulation.

Once this array was defined, the measured tooth angles were specified in an index array with each entry given by the ratio $\phi/\Delta\phi$ rounded to the nearest integer, where ϕ is the measured angle of the tooth at the selected z location. This index array was then used to specify the angle of any tooth at any z location by identifying the nearest preselected value from the closely spaced tooth angle array for use in the simulation. The reason for this approach is that the current chip thickness in milling depends not only on the commanded chip thickness and current vibration, but also the surface left by the previous teeth at the current tooth angle. To be able to do so conveniently, this information was organized according to specified tooth angles.

The radius variation for each insert was included as runout, RO. The z-dependent RO values for each of the 15 inserts were also arranged in an array, where the columns were the individual teeth (i.e., the collection of five inserts) and the rows were the z locations (again in steps of 0.1 mm). All RO values were normalized to the maximum radius from all 15 inserts, which yielded negative RO values. A negative RO value reduces the chip thickness for the current tooth, but leaves behind material that the next tooth must remove (and therefore increases that chip thickness).

Two other data organization requirements were: 1) the surface that was left behind by the current tooth; and 2) the commanded chip thickness. To keep track of the previously machined surface, another array was defined that recorded the surface location in the tool's normal direction for each simulation time step. The columns of this matrix were the number of steps per revolution and the rows were the z locations. The influence of runout on subsequent chip thickness values was captured in this matrix. Because there were variations in the tooth angles from one insert to the next, the commanded chip thickness was also modified to account for the actual tooth angle using the circular tooth path approximation. This approximation calculates the nominal chip thickness from the product of the feed per tooth and the sine of the tooth angle.

Given this information, the simulation proceeded as follows:
1. 1. The instantaneous chip thickness, $h(t)$, was determined using the commanded chip thickness, runout, and vibration of the current and previous teeth at the selected tooth angle.
2. The cutting force components in the tangential, t, and normal, n, directions were calculated at each axial slice using:

$$F_t(t) = k_{tc}bh(t) + k_{te}b \qquad (1)$$

$$F_n(t) = k_{nc}bh(t) + k_{ne}b \qquad (2)$$

where b is the slice width (0.1 mm) and the cutting force coefficients are identified by the subscripts: t or n for direction; and c or e for cutting or edge effect. These forces were then summed over all axial slices engaged in the cut.
3. The summed force components were used to find the new displacements by numerical solution of the differential equations of motion in the x (feed) and y directions:

$$m_x\ddot{x} + c_x\dot{x} + k_x x = F_t(t)\cos\phi + F_n(t)\sin\phi \qquad (3)$$

$$m_y\ddot{y} + c_y\dot{y} + k_y y = F_t(t)\sin\phi - F_n(t)\cos\phi \qquad (4)$$

where m is the modal mass, c is the modal viscous damping coefficient, and k is the modal stiffness. The subscripts identify the direction and multiple degrees-of-freedom in each direction can be accommodated.
4. The tool rotation angle was incremented by adding one to each entry in the tooth angle index array and the process was repeated.

A flowchart is provided in Fig. 10 to summarize the simulation steps.
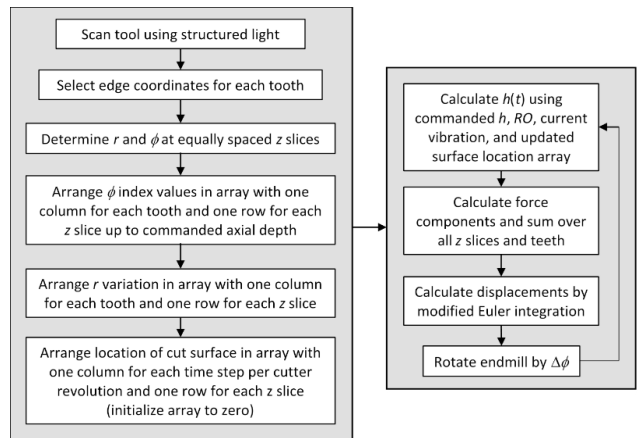
Figure 10: Time domain simulation flowchart. (Left) setup information. (Right) simulation steps.

6. Force modeling

There are two options for determining the force model coefficients in Eqs. 1 and 2. First, cutting tests may be completed where the axial depth, radial depth, and feed per tooth values are prescribed, the force components are measured for the desired tool-work material pair using a cutting force dynamometer, and a linear regression is completed to calculate

the force coefficients [1-2, 21]. Second, finite element simulation may be applied to predict the cutting force components using the work material's constitutive relationship (e.g., the Johnson-Cook model [22]) and machining parameters. The second was selected for this digital study, where orthogonal cutting simulations were completed using AdvantEdge™ from Third Wave Systems [23].

The Johnson-Cook flow stress model has been widely studied in the literature. See Eq. 5, where σ is the equivalent stress, ε is the equivalent plastic strain, $\dot{\varepsilon}$ is the strain rate, T is the deformation temperature, and T_m is the melt temperature. The material parameters are A, B, C, n, and m, where A is the yield strength of the material under reference conditions, B is the strain hardening constant, C is the strain rate strengthening coefficient, n is the strain hardening coefficient, and m is the thermal softening coefficient. Also, $\dot{\varepsilon}_{ref}$ and T_{ref} are the reference strain rate (typically set to 1) and the reference deformation temperature (typically set to 20 deg C). Multiple authors report the Eq. 5 parameters for 6061-T6 aluminum [24-33], the workpiece material selected for this study. A summary of these values is provided in Table 1.

$$\sigma = (A + B\varepsilon^n)\left(1 + C\ln\left(\frac{\dot{\varepsilon}}{\dot{\varepsilon}_{ref}}\right)\right)\left(1 - \left(\frac{T-T_{ref}}{T_m-T_{ref}}\right)^m\right) \quad (5)$$

Table 1: Johnson-Cook flow stress model parameters.

A (MPa)	B (MPa)	C	n	m	Ref.
324	114	0.002	0.42	1.34	24
250	79.7	0.0249	0.499	1.499	24
293.4	121.26	0.002	0.23	1.34	25
324.1	113.8	0.002	0.42	1.34	26
250	70	0.001	0.499	1	27
250	79	0.0249	0.499	1.499	27
250	137	0.0205	0.499	1.499	27
250	209	0.001	0.499	1.499	27
275	86	-	0.39	1	28
324	114	0.002	0.42	1.34	28
335	85	0.012	0.11	1	28
250	79.7	0.0249	0.499	1.499	28
324	114	0.002	0.42	1.34	29
236.7	41.2	0.0411	0.084	1.41	30
293.4	121.26	0.002	0.23	1.34	30
324	114	0.002	0.42	1.34	30
275	86	0.0031	0.39	1	31
324	114	0.002	0.42	1.34	31
324	114	0.002	0.42	1.34	32
164	211	0.00197	0.465	1.419	32
293	121.26	0.002	0.23	1.34	33
324	114	0.002	0.42	1.34	33
282.9	109.1	0.0081	0.3905	1.321	Mean
42.9	39.2	0.0114	0.1252	0.164	Std.

The final two rows of Table 1 give the mean and standard deviation values for the five parameters. To calculate the four cutting force coefficients in Eqs. 1 and 2, the following procedure was followed:

1. Values for A, B, C, n, and m were randomly sampled from normal distributions centered at the mean value with one standard deviation (Table 1).

2. The sampled 6061-T6 aluminum Johnson-Cook material model was defined manually in AdvantEdge™. The tool material was set as carbide and the AdvantEdge™ carbide material model was used.

3. The cutting edge cross-sectional geometry was imported as a series of points that defined the rake and relief surface profiles (see Figs. 8 and 9).

4. The orthogonal cutting parameters were specified including the cutting speed, chip width, and chip thickness. The cutting speed was defined using the spindle speed (4800 rpm) and endmill radius (15.88 mm); the chip width was set to 1 mm for scaling convenience. The mean chip thickness was selected to be {0.13, 0.14, 0.15, 0.16, or 0.17} mm; 0.15 mm was the feed per tooth used in the follow-on milling experiments. The Coulomb friction coefficient was left at the default value of 0.5.

5. The five simulations at the five different chip thickness values were completed and the mean tangential, F_t, and surface normal direction, F_n, force values were recorded (initial transients at the cut entry and final transients at the cut exit were excluded).

6. The ratio of the five cutting force values to the chip width, or F/b, were plotted on the ordinate and the five chip thickness values were plotted on the abscissa. The slope and intercept were determined from a linear regression to the five data pairs. For each direction, the slope provided the c coefficient and the intercept identified the e coefficient [1-2].

Steps 1-6 were repeated 25 times for 25 different {A, B, C, n, m} combinations (zero correlation was assumed between the five parameters). This required 125 total simulations given the five chip thickness values for each combination; the execution time for each simulation was approximately one hour. The results from this exercise are summarized in Table 2. Note that these values are specific to the tool/insert edge geometry (Figs. 8 and 9), Johnson-Cook material model parameters and distributions (Table 1), and, to a lesser extent, the machining parameters.

Table 2: Cutting force model coefficients.

Coefficient	Mean	Standard deviation
k_{tc}	644.5 N/mm^2	89.3 N/mm^2
k_{te}	33.2 N/mm	5.3 N/mm
k_{nc}	276.7 N/mm^2	46.7 N/mm^2
k_{ne}	48.9 N/mm	9.1 N/mm

7. Sensitivity analysis

To build on the previous finite element results, a sensitivity analysis was performed to identify the relative contributions of the distributions in {A, B, C, n, and m} to variation in the tangential and normal force components. To determine the individual contributions, one parameter distribution was sampled while holding the other four parameters at their mean values. The standard deviation in the predicted force components was then due solely to variation in the selected Johnson-Cook parameter.

For this exercise, 25 samples were randomly sampled from a single parameter's normal distribution (see Table 1). Simulations were completed using the sampled parameter and the remaining four mean parameters at five chip thickness values {0.13, 0.14, 0.15, 0.16, and 0.17} mm for a total of 125 simulations. The mean and standard deviation for both force directions (tangential and normal) were calculated. The ratio of the standard deviation to mean force was then plotted for each parameter in the two directions. The results are displayed in Figs. 11 and 12. It is observed that B is the most sensitive parameter for the tangential direction and A is the most sensitive parameter for the normal direction.
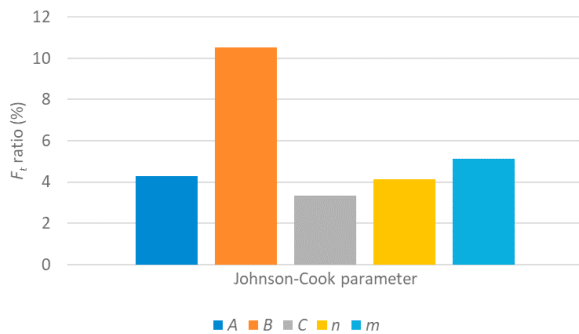

Figure 11: Sensitivity analysis for tangential direction force. The ratio of the standard deviation in the force when varying a single parameter to the mean force value is plotted on the vertical axis.
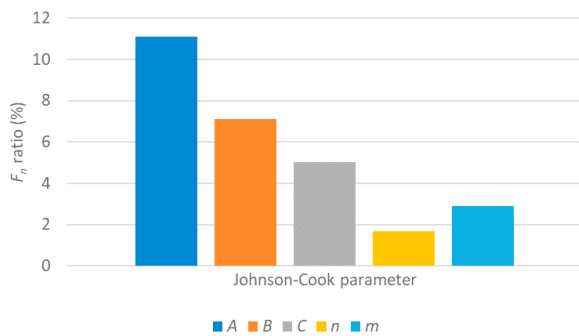

Figure 12: Sensitivity analysis for normal direction force. The ratio of the standard deviation in the force when varying a single parameter to the mean force value is plotted on the vertical axis.

8. Tool tip FRF

The Kennametal indexable endmill was inserted in a Techniks CAT40xER50 – 4" collet holder with an extension length of 52.6 mm. The tool-holder was clamped in the spindle of a Makino a51nx four-axis, horizontal spindle CNC milling machine and the tool tip FRF was measured by impact testing. In this case, an instrumented hammer was used to excite the assembly and the response was measured with a low-mass accelerometer. Fitting was then performed to extract the modal parameters from the FRF. The modal parameters are tabulated in Appendix A and the tool tip FRF is displayed in Fig. 13.
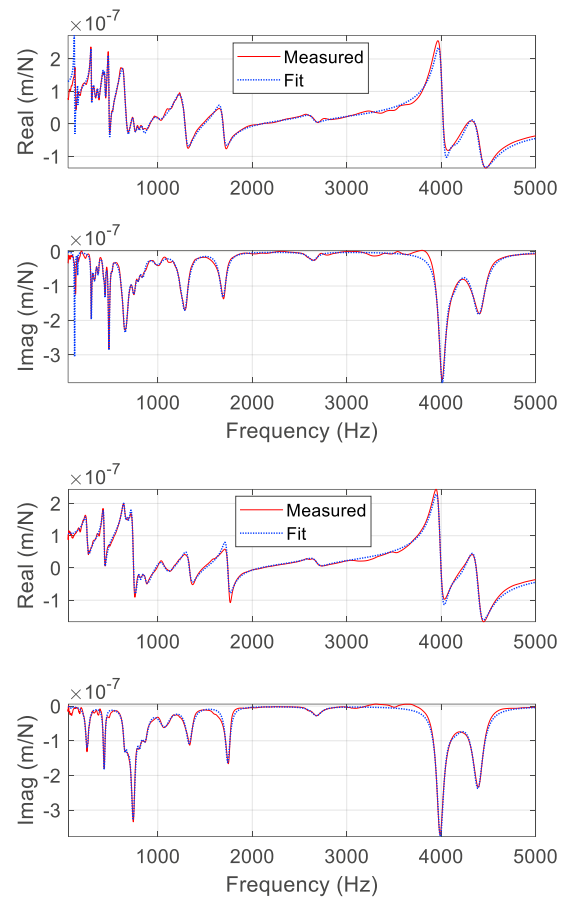

Figure 13: Tool tip FRFs for the (left) x and (right) y directions. The (top) real and (bottom) imaginary parts of the complex-valued FRFs are presented.
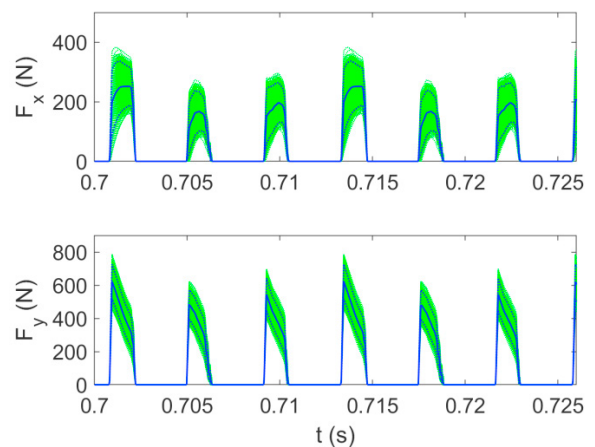

Figure 14: Monte Carlo simulation output for the (top) x direction force, F_x, and (bottom) y direction force, F_y. The force profiles for 1000 iterations are shown by the thin green dotted lines. The mean value is given by the heavy blue solid lines. The 95% confidence interval (mean ± two standard deviations) is identified by the heavy blue dotted lines.

9. Uncertainty propagation

As noted, the Johnson-Cook model parameters were randomly sampled from normal distributions defined by a literature

review and these random samples were used to identify the corresponding distribution in mechanistic force model coefficients by finite element simulation; see Table 2. The milling time domain simulation was then embedded within a Monte Carlo simulation, where the Table 2 force model coefficients were randomly sampled and *x* (feed) and *y* direction time-dependent force profiles were predicted for each set of coefficients (zero correlations was assumed between the four coefficients when sampling). The tool tip FRFs were held constant. Example results from 1000 iterations are provided in Fig. 14, where the axial depth is 5 mm, the radial depth is 3.18 mm (10% radial immersion), and the spindle speed is 4800 rpm for the down (climb) milling operation.

10. Cutting force comparison

Cutting trials were completed on the Makino a51nx CNC milling machine. The 6061-T6 aluminum workpiece was mounted on a cutting force dynamometer (Kistler 9257B) and the endmill was clamped in the ER50 collet holder and inserted in the CAT-40 spindle interface; see Fig. 15. Tests were performed at axial depths of cut from 5 mm to 20 mm. The commanded feed per tooth for these down (climb) milling experiments was 0.150 mm, the spindle speed was 4800 rpm, and the radial depth of cut was 3.18 mm (10% radial immersion).

Measured and predicted *x* (feed) and *y* direction force values for *b* = {5, 10, 15, and 20} mm are shown in Figs. 16-19, where the mean and 95% confidence interval are presented for each prediction. Good agreement between the measurement and mean is observed at all four axial depths for F_x. However, the measured F_y appears at or below the confidence interval in each case. For the 5 mm axial depth, cutting occurs with a single row of inserts (A in Fig. 1). Two revolutions of data are displayed, so six peaks are observed – one for each of the three inserts for both revolutions. At 10 mm, the second row of inserts (B in Fig. 1) just begins to engage so additional peaks begin to emerge in the measured profiles. At 15 mm, insert row B is fully engaged so 12 peaks are seen over the two revolutions of data. For the 20 mm axial depth, insert row C begins cutting. The complicated, uneven force profiles in Figs. 13-16 are a product of both the indexable endmill geometry and runout.
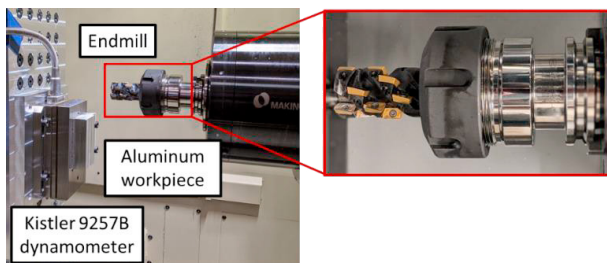

Figure 15: Experimental setup for milling tests.

Measured and predicted *x* (feed) and *y* direction force values for *b* = {5, 10, 15, and 20} mm are shown in Figs. 16-19, where the mean and 95% confidence interval are presented for each prediction. Good agreement between the measurement and mean is observed at all four axial depths for F_x. However, the measured F_y appears at or below the confidence interval in each case. For the 5 mm axial depth, cutting occurs with a single row

of inserts (A in Fig. 1). Two revolutions of data are displayed, so six peaks are observed – one for each of the three inserts for both revolutions. At 10 mm, the second row of inserts (B in Fig. 1) just begins to engage so additional peaks begin to emerge in the measured profiles. At 15 mm, insert row B is fully engaged so 12 peaks are seen over the two revolutions of data. For the 20 mm axial depth, insert row C begins cutting. The complicated, uneven force profiles in Figs. 16-19 are a product of both the indexable endmill geometry and runout.
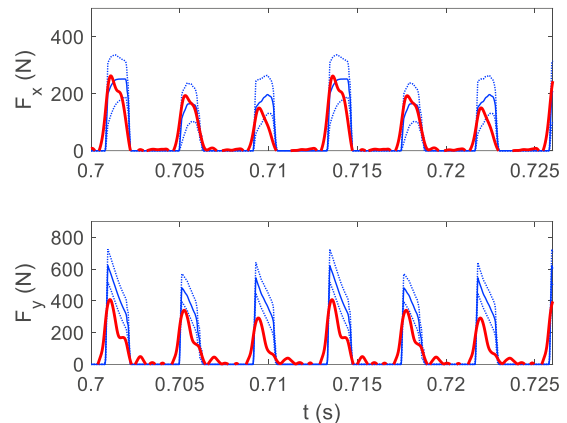

Figure 16: Comparison of measured (heavy red solid line) and predicted mean (thin blue solid line) and 95% confidence interval (thin blue dotted lines) for forces in the (top) *x* and (bottom) *y* directions; the axial depth is 5 mm and the feed per tooth is 0.150 mm.

Figure 17: Comparison of measured (heavy red solid line) and predicted mean (thin blue solid line) and 95% confidence interval (thin blue dotted lines) for forces in the (top) *x* and (bottom) *y* directions; the axial depth is 10 mm and the feed per tooth is 0.150 mm.
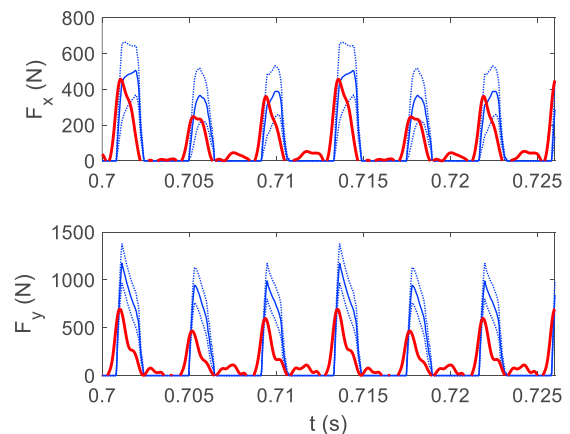
Figure 18: Comparison of measured (heavy red solid line) and predicted mean (thin blue solid line) and 95% confidence interval (thin blue dotted lines) for forces in the (top) x and (bottom) y directions; the axial depth is 15 mm and the feed per tooth is 0.150 mm.

Figure 20: Comparison of measured (heavy red solid line) and predicted mean (thin blue solid line) and 95% confidence interval (thin blue dotted lines) for forces in the (top) x and (bottom) y directions; the axial depth is 5 mm and the feed per tooth is 0.050 mm.
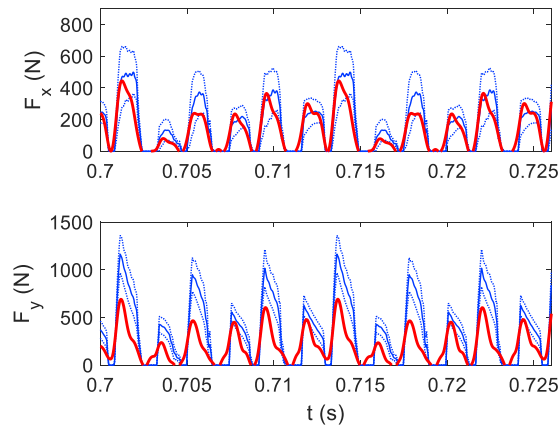

Figure 19: Comparison of measured (heavy red solid line) and predicted mean (thin blue solid line) and 95% confidence interval (thin blue dotted lines) for forces in the (top) x and (bottom) y directions; the axial depth is 20 mm and the feed per tooth is 0.150 mm.
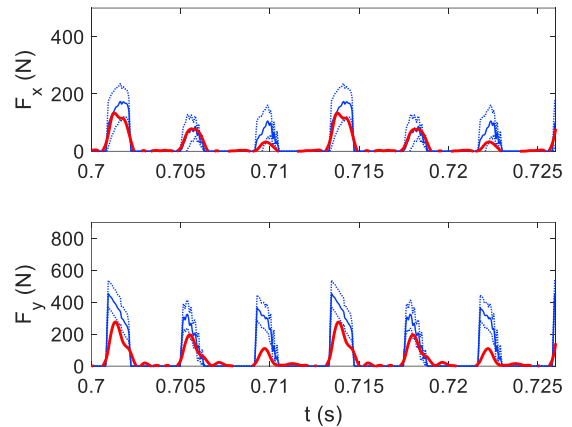

Figure 21: Comparison of measured (heavy red solid line) and predicted mean (thin blue solid line) and 95% confidence interval (thin blue dotted lines) for forces in the (top) x and (bottom) y directions; the axial depth is 5 mm and the feed per tooth is 0.075 mm.
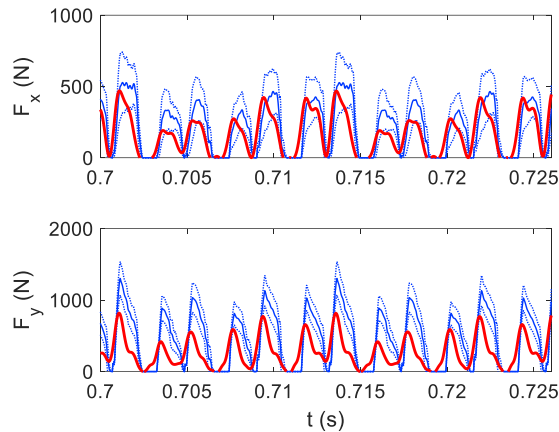
Finally, the axial depth was held constant at 5 mm and the feed per tooth value was varied {0.050, 0.075, 0.100, 0.125, and 0.150 mm}. The first four results are displayed in Figs. 20-23, while the 0.150 mm result was already shown in Fig. 16. As expected, the force level grows with increasing chip thickness without changing the overall profile (three peaks per revolution) since the axial depth is constant. As with the varying axial depth experiments, the measured x direction force matches predicted mean, while the measured y direction force is below the 95% confidence interval.

Figure 22: Comparison of measured (heavy red solid line) and predicted mean (thin blue solid line) and 95% confidence interval (thin blue dotted lines) for forces in the (top) x and (bottom) y directions; the axial depth is 5 mm and the feed per tooth is 0.100 mm.
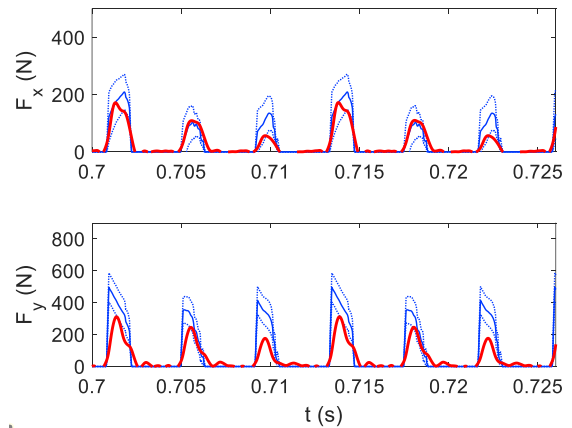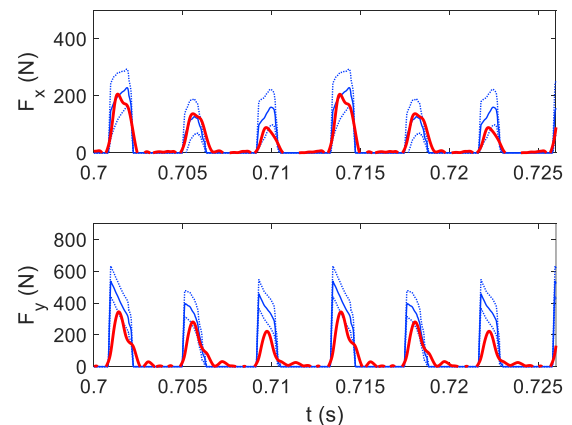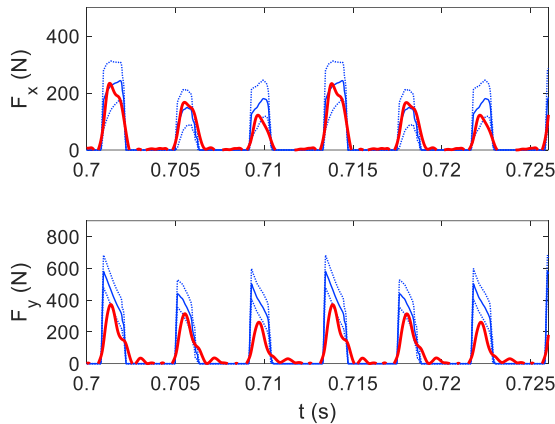
Figure 23: Comparison of measured (heavy red solid line) and predicted mean (thin blue solid line) and 95% confidence interval (thin blue dotted lines) for forces in the (top) x and (bottom) y directions; the axial depth is 5 mm and the feed per tooth is 0.125 mm.

To conclude the force comparison, the four cutting force coefficients from Eqs. 1 and 2 were identified experimentally. Down milling tests were completed at 4800 rpm, 3.18 mm radial depth, 5 mm axial depth, and five feed per tooth values with the 6061-T6 workpiece mounted on a Kistler 9257B dynamometer. The mean force in the x (feed) and y directions was plotted against the commanded feed per tooth and linear regressions were completed to identify the slope and intercept values. These were then used to determine the cutting force coefficients as detailed in [1-2]. A comparison between the experimental and digital coefficients is provided in Table 3. The percent difference relative to the experimental results is also included.

Table 2: Comparison of cutting force model coefficients.

Coefficient	J-C model and FE simulation	Experimental	Percent difference relative to experimental
k_{tc}	644.5 N/mm^2	874 N/mm^2	-26.3%
k_{te}	33.2 N/mm	18.6 N/mm	78.5%
k_{nc}	276.7 N/mm^2	255 N/mm^2	8.5%
k_{ne}	48.9 N/mm	1.57 N/mm	3015%

The measured force profiles for the 5 mm axial depth, 0.150 mm feed per tooth case are superimposed on the predicted force profiles using the cutting force coefficients determined from: 1) the Johnson-Cook model/finite element simulation; and 2) experimental mean force linear regression in Fig. 24. It is observed that the x direction force is overpredicted by the experimental coefficients, while the y direction force matches the measured force. Effectively, the errors have been reversed between the two force models in Table 3 so it is not clear that either is more accurate.

11. Conclusions

This paper provided an integrated digital framework for modeling cutting force in milling. Structured light scanning was used to produce a model of an example (indexable) endmill. From this model, spatial coordinates for the points that

define the insert cutting edges were extracted. The points were used to determine the cutting edge radius and angle at equally spaced points along the tool's axis. Additionally, the rake and relief profiles for the insert's cross-section were measured and used in commercially-available finite element analysis software to predict the force components for orthogonal cutting. The cutting force coefficients were calculated using the finite element force predictions. The tool tip frequency response function was measured. The digital cutting edge geometry, tool tip frequency response, and force model coefficients were then incorporated in a time domain simulation that was used to predict cutting force for user-selected operating parameters.
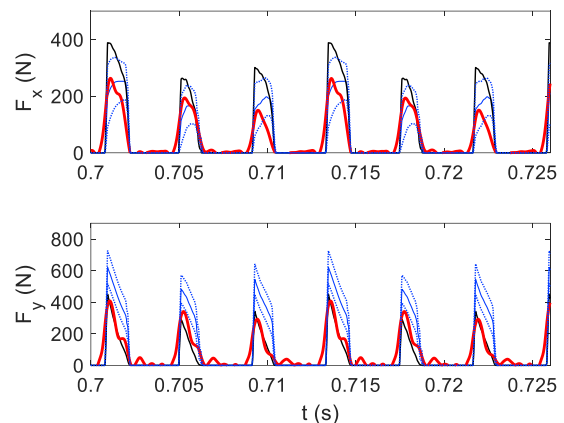

Figure 24: Comparison of measured (heavy red solid line) and predicted mean forces using cutting force coefficients obtained from: 1) Johnson-Cook model/finite element simulation (thin blue solid line) with 95% confidence intervals (thin blue dotted lines); and 2) experimental mean force linear regression (thin black line). The top panel shows the x direction force, while the bottom panel displays the y direction force. The axial depth is 5 mm and the feed per tooth is 0.150 mm.

Given this digital framework, the uncertainty in 6061-T6 aluminum Johnson-Cook flow stress model parameters were propagated to, first, the uncertainty in the corresponding mechanistic cutting force model obtained by orthogonal cutting finite element simulation and, second, the uncertainty in the milling force predicted by time domain simulation. This process incorporated five key steps: 1) a literature review was completed to identify the means and standard deviations for the 6061-T6 aluminum Johnson-Cook model parameters; 2) structured light scanning was used to measure an endmill's cutting edge macro-geometry along the tool axis; 3) structured light scanning was used to identify the cutting edge cross-sectional rake and relief profiles for the same endmill; 4) AdvantEdge™ orthogonal cutting finite element analysis was applied to determine the mechanistic force model coefficients using the measured rake and relief profiles and random samples from the Johnson-Cook parameter distributions; and 5) time domain simulation was completed with inputs that included the measured cutting edge macro-geometry, finite element-based force model with uncertainty, and measured structural dynamics. Distributions of milling force predictions were determined by Monte Carlo simulation and compared to in-

process measurements for an indexable endmill-collet holder to demonstrate the approach.

Key observations included the following.

- There is significant variation in Johnson-Cook flow stress model parameters reported in the literature. The percent fractions of the standard deviation to the mean for the five Johnson Cook parameters were: A – 15.2%, B – 35.9%, C – 140.7%, n – 32.1%, and m – 12.4%.
- A sensitivity analysis revealed that B was the key parameter for accurate tangential force component prediction and A was the key parameter for accurate normal force component prediction in orthogonal cutting.
- The measured x direction (feed) force agreed with the predicted mean for 10% radial immersion down milling conditions.
- The measured y direction force was at the lower limit of the 95% confidence interval for 10% radial immersion down milling conditions.

The force predictions based on the Johnson-Cook flow stress model performed as well as predictions based on a calibrated force model using a linear regression to measured mean cutting forces over a range of chip thickness values.

Acknowledgements

References

[1]   Schmitz, T.L. and Smith, K.S., 2019. Machining Dynamics: Frequency Response to Improved Productivity, 2nd Ed., Springer, New York.
[2]   Altintas, Y., 2012. Manufacturing Automation: Metal Cutting Mechanics, Machine Tool Vibrations, and CNC Design, Cambridge University Press.
[3]   Altintas, Y. and Weck, M., 2004. Chatter stability of metal cutting and grinding. CIRP Annals-Manufacturing Technology, 53(2), pp.619-642.
[4]   https://www.weforum.org/reports/the-impact-of-covid-19-on-the-future-of-advanced-manufacturing-and-production-insights-from-the-world-economic-forum-s-global-network-of-advanced-manufacturing-hubs.
[5]   Fu, H.J., DeVor, R.E. and Kapoor, S.G., 1984. A mechanistic model for the prediction of the force system in face milling operations. Journal of engineering for industry, 106(1), pp.81-88.
[6]   Kim, H.S. and Ehmann, K.F., 1993. A cutting force model for face milling operations. International Journal of Machine Tools and Manufacture, 33(5), pp.651-673.
[7]   Zheng, H.Q., Li, X.P., Wong, Y.S. and Nee, A.Y.C., 1999. Theoretical modelling and simulation of cutting forces in face milling with cutter runout. International Journal of Machine Tools and Manufacture, 39(12), pp.2003-2018.
[8]   Engin, S. and Altintas, Y., 2001. Mechanics and dynamics of general milling cutters: Part II: Inserted cutters. International Journal of Machine Tools and Manufacture, 41(15), pp.2213-2231.
[9]   Altintas, Y. and Engin, S., 2001. Generalized modeling of mechanics and dynamics of milling cutters. CIRP Annals, 50(1), pp.25-30.
[10] Wang, J.J.J. and Yang, C.S., 2003. Angle and frequency domain force models for a roughing end mill with a sinusoidal edge profile.

[11] International Journal of Machine Tools and Manufacture, 43(14), pp.1509-1520.
[11] Merdol, S.D. and Altintas, Y., 2004. Mechanics and dynamics of serrated cylindrical and tapered end mills. Journal of Manufacturing Science and Engineering, 126(2), pp.317-326.
[12] Dombóvári, Z., Altintas, Y. and Stépán, G., 2010. The effect of serration on mechanics and stability of milling cutters. International Journal of Machine Tools and Manufacture, 50(6), pp.511-520.
[13] Dombóvári, Z., Munoa, J. and Stépán, G., 2012. General milling stability model for cylindrical tools. Procedia CIRP, 4, pp.90-97.
[14] Stépán, G., Munoa, J., Insperger, T., Surico, M., Bachrathy, D. and Dombóvári, Z., 2014. Cylindrical milling tools: comparative real case study for process stability. CIRP Annals, 63(1), pp.385-388.
[15] Koca, R. and Budak, E., 2013. Optimization of serrated end mills for reduced cutting energy and higher stability. Procedia CIRP, 8, pp.570-575.
[16] Grabowski, R., Denkena, B. and Köhler, J., 2014. Prediction of process forces and stability of end mills with complex geometries. Procedia CIRP, 14, pp.119-124.
[17] Tehranizadeh, F. and Budak, E., 2017. Design of serrated end mills for improved productivity. Procedia CIRP, 58, pp.493-498.
[18] No, T., Gomez, M., Copenhaver, R., Perez, J.U., Tyler, C. and Schmitz, T.L., 2019. Force and stability modeling for non-standard edge geometry endmills. Journal of Manufacturing Science and Engineering, 141(12).
[19] No, T., Gomez, M., Copenhaver, R., Perez, J.U., Tyler, C. and Schmitz, T.L., 2019. Scanning and modeling for non-standard edge geometry endmills. Procedia Manufacturing, 34, pp.305-315.
[20] Smith, K.S. and Tlusty, J., 1991. An overview of modeling and simulation of the milling process. ASME Journal of Engineering for Industry, 113(2), pp.169-175.
[21] Rubeo, M. and Schmitz, T., 2016. Milling force modeling: A comparison of two approaches. Procedia Manufacturing, 5, pp.90-105.
[22] Johnson G. R. and Cook W. H., 1983. A constitutive model and data for metals subjected to large strains, high strain rates and high temperatures. In: 7th International Symposium on Ballistics, pp.514-546.
[23] https://www.thirdwavesys.com/advantedge/.
[24] Akram, S., Jaffery, S.H.I., Khan, M., Fahad, M., Mubashar, A. and Ali, L., 2018. Numerical and experimental investigation of Johnson-Cook material models for aluminum (Al 6061-T6) alloy using orthogonal machining approach. Advances in Mechanical Engineering, 10(9), pp.1-14.
[25] Adibi-Sedeh, A.H., Madhavan, V. and Bahr, B., 2003. Extension of Oxley's analysis of machining to use different material models. Journal of Manufacturing Science and Engineering, 125(4), pp.656-666.
[26] Boldyrev, I.S., Shchurov, I.A. and Nikonov, A.V., 2016. Numerical simulation of the aluminum 6061-T6 cutting and the effect of the constitutive material model and failure criteria on cutting forces' prediction. Procedia Engineering, 150, pp.866-870.
[27] Daoud, M., Jomaa, W., Chatelain, J.F. and Bouzid, A., 2014. A machining-based methodology to identify material constitutive law for finite element simulation. The International Journal of Advanced Manufacturing Technology, 77(9-12), pp.2019-2033.
[28] Daoud, M., Jomaa, W., Chatelain, J.F., Bouzid, A. and Songmene, V., 2014. Identification of material constitutive law constants using machining tests: A response surface methodology based approach. High Performance and Optimum Design of Structures and Materials, 137.
[29] Fang, N., 2005. A new quantitative sensitivity analysis of the flow stress of 18 engineering materials in machining. Journal of Engineering Materials and Technology, 127(2), pp.192-196.
[30] Fernandez-Zelaia, P. and Melkote, S.N., 2019. Statistical calibration and uncertainty quantification of complex machining computer models. International Journal of Machine Tools and Manufacture, 136, pp.45-61.
[31] Pittalà, G.M. and Monno, M., 2009. 3D finite element modeling of face milling of continuous chip material. The International Journal of Advanced Manufacturing Technology, 47(5-8), pp.543-555.
[32] Rule, W.K., 1997. A numerical scheme for extracting strength model coefficients from Taylor test data. International Journal of Impact Engineering, 19(9-10), pp.797-810.
[33] Zaghbani, I. and Songmene, V., 2009. A force-temperature model including a constitutive law for dry high speed milling of aluminium

alloys. Journal of Materials Processing Technology, 209(5), pp.2532-2544.

Appendix A: Modal parameters from tool tip frequency response function measurements

Table A1: Modal parameters for *x* direction.

Mode number	Natural frequency (Hz)	Stiffness (N/m)	Damping ratio (%)
1	119	0.0571×10^9	2.88
2	152	0.5484×10^9	1.43
3	296	0.1810×10^9	1.59
4	329	0.1182×10^9	5.66
5	368	0.4768×10^9	2.30
6	425	0.5756×10^9	1.94
7	441	0.2978×10^9	1.62
8	483	0.1092×10^9	1.71
9	514	1.0637×10^9	1.89
10	655	0.0423×10^9	5.34
11	681	2.2135×10^9	1.54
12	748	0.1650×10^9	3.60
13	795	0.7147×10^9	2.07
14	843	0.2800×10^9	3.42
15	1000	0.2911×10^9	6.03
16	1233	1.0197×10^9	2.60
17	1285	0.0873×10^9	3.55
18	1690	0.1591×10^9	2.44
19	2642	0.9292×10^9	2.21

Table A2: Modal parameters for *y* direction.

Mode number	Natural frequency (Hz)	Stiffness (N/m)	Damping ratio (%)
20	4013	0.1328×10^9	1.08
21	4129	0.3522×10^9	2.14
22	4399	0.1520×10^9	1.92
1	83	1.0330×10^9	11.01
2	252	0.0537×10^9	7.93
3	432	0.1111×10^9	2.56
4	650	0.2460×10^9	2.51
5	682	0.2417×10^9	3.22
6	739	0.0470×10^9	3.55
7	808	0.3994×10^9	2.37
8	865	0.1352×10^9	4.78
9	1073	0.1501×10^9	6.37
10	1332	0.1588×10^9	3.09
11	1740	0.1832×10^9	1.71
12	2680	0.7866×10^9	2.44
13	3991	0.1294×10^9	1.10
14	4142	0.3616×10^9	2.94
15	4389	0.1520×10^9	1.47